ROYAL SOCIETY OF CHEMISTRY

PAPER

Check for updates

Energetic description of the liquid–vapor interface of water with organic coating molecules

Julien Devémy, [iD] [a] Alain Dequidt, [iD] [a] Pascal Renard, [iD] [b]
Laurent Deguillaume [iD] [bc] and Patrice Malfreyt [iD] *[a]

In situ measurements revealed the presence of a myriad of organic chemical compounds in cloud droplets. Among them, a significant fraction is composed of polar or amphiphilic compounds and these compounds have been detected in various contrasting environments (marine, biogenic, urban areas). This raises a simple question of their spatial positioning in a cloud droplet. Previous study suggested they can form an organic surface coating at the air/water interface, thus potentially perturbing the exchanges of molecules between the gaseous and aqueous phases. The present work aims at investigating the properties of the water surface at the molecular scale by selecting 4 organic compounds representative of the molecular diversity observed in clouds. Two fatty acids (*cis*-pinonic acid and nonanoic acid) commonly detected in the atmosphere (aerosol particles and cloud waters) were chosen. Levoglucosan is an anhydro sugar ubiquitous in the air and well-known as a tracer of biomass burning. Finally, oxalic acid, one of the most abundant di-acids in the atmosphere, has been chosen. Its ability to form a coating film was analyzed through the calculation of a free energy profile along the direction normal to the surface of water. Nonanoic and *cis*-pinonic acids have been shown to partition to the surface, in contrast to levoglucosan and oxalic acid that remain in water. The surface tension of the liquid–vapor (LV) interface of water was calculated as a function of surface excess of nonanoic and *cis*-pinonic acids. We completed this study by examining how the presence of a hydrophobic monolayer of nonanoic molecules at the surface of water can change the behavior of a hydrophilic molecules such as levoglucosan at the interface. Our results clearly indicate that levoglucosan molecules in the gas phase can be adsorbed on this organic layer. Results from this study are of particular interest for atmospheric research since by confirming the concept of organic film formation at the air/droplet interface, they lead to questions about possible heterogeneous reactivity phenomena and potential modification of compound exchanges between the gas and aqueous phases.

1 Introduction

The water–air interface or in a more generic way liquid–vapor interface is ubiquitous in the environment. It is found at the surface of oceans and lakes, on atmospheric aerosols, fog/cloud droplets[1] and in the human respiratory system. Even if the interfacial region bridges the bulk water liquid phase and the gas phase, it may have energetic and structural characteristics that are quite different from those of homogeneous phases due to the reduction in dimensionality.

From a molecular viewpoint, the water–air interfacial region shows a density gradient leading to some significant changes in the orientation of water molecules and the organization of the hydrogen bond network. From thermodynamic considerations, the attractive forces acting on molecules at the interface are anisotropic, whereas there is a perfect force balance due to the symmetry around the molecules in the bulk phases.[2] This anisotropy in the intermolecular interactions is at the origin of the surface tension which is equal to 72 mN m^{-1} for water at 298 K.[3–5]

Atmospheric humid aerosol particles and fog/cloud droplets in the atmosphere are perfect examples of the creation of complex air/water interfaces. They present extremely diverse chemical compositions resulting from emissions of numerous natural and/or anthropogenic sources. They are especially composed of a complex mixture of organic components.[6,7] Among those compounds, a significant fraction is composed of polar or amphiphilic

[a] Université Clermont Auvergne, CNRS, Clermont Auvergne INP, Institut de Chimie de Clermont-Ferrand, F-63000 Clermont-Ferrand, France.
E-mail: Patrice.Malfreyt@uca.fr
[b] Université Clermont Auvergne, CNRS, Clermont Auvergne INP, Laboratoire de Météorologie Physique, F-63000 Clermont-Ferrand, France
[c] Université Clermont Auvergne, CNRS, Clermont Auvergne INP, Observatoire de Physique du Globe de Clermont-Ferrand, F-63000 Clermont-Ferrand, France

compounds.[8] For example, about 150 polar organic compounds have been identified in urban atmospheric aerosols.[9] Some of these organic compounds, called surface-active agents, can significantly reduce the surface tension of the water–air interface.[10,11] By impacting on the surface physical properties of the aerosols, these compounds modify the life cycle of these particles which can have negative effects on air quality, ecosystems, health and climate on Earth.[12]

At the air/water interface, organic compounds can also form an organic film possibly favoring chemical reactions and physical transformations compared to bulk solutions,[13–16] especially when the reactants are organic species with hydrophobic groups. For instance, the presence of this organic coating can modify the photo-reactivity,[17] increase the interfacial adsorption,[18] and hinder the transport of trace gases through the interfacial region[19] However, the amount and distribution of the hydrophobic molecules at the surface of the air/water interface are difficult to access experimentally. To overcome this problem, numerical models were developed to reproduce multiphasic inorganic and organic reactivity together with the mass transfer of molecules between the gaseous and the aqueous phases.[20] However, these models of various complexity do not consider any possibility that this transfer can be perturbed by the presence of molecules at the surface of the droplets. One solution for enriching numerical models in the molecular and energetic descriptions of the air/water interface is to carry out molecular simulations of the air/water interface. Additionally, these molecular simulations should enable experimental measurements to be better interpreted in terms of the microscopic view they provide. Indeed, it is very important to investigate how the presence of organic molecules in water impacts on the molecular-level structure of the water–air interface and on the surface tension of the coated humid aerosols or cloud droplets.

Among the myriad of organic compounds detected in aerosols and cloud waters, we decided to select a few polar molecules as a proxy to study how they position at the air/water interface. Levoglucosan (1,6-anhydro-β-D-glucopyranose) is a major component of aerosol particles[21] and a product of cellulose combustion; it is therefore recognized as a molecular source tracer of biomass burning[22] and is suspected to play a role in the chemistry at the air/water interface.[23] cis-Pinonic acid, a monocarboxylic acid, is formed by photooxidation of α-pinene and β-pinene. It has been shown by molecular simulations[10] on water droplets that the addition of cis-pinonic acid molecules reduces the surface tension. Li et al.[10] have also established a strong dependence of the surface tension on the water droplet radius. Ab initio and thermochemical calculations carried out by Hou et al.[24] revealed that mono- or di-hydrated clusters of the cis-pinonate anion are more stable than larger clusters. Nonanoic acid (NA), which can be classified in the family of medium-chain fatty acids, is a highly surface-active simple organic acid for aerosols. Finally, oxalic acid has been

chosen; it is the smallest dicarboxylic acid and is a highly abundant organic compound in the atmosphere.[25] The adsorption of oxalic acid molecules on the surface of hexagonal ice, carried out by molecular simulations,[26] has shown a peak of adsorption at the surface of water at temperatures lower than 240 K. Interestingly, Darvas et al. pointed out that the desorption process has already started at 240 K with a partial hydration of the oxalic acid aggregates. These authors[27] have also investigated by molecular simulations the nucleation around small oxalic acid aggregates at two compositions at temperatures ranging from 200 to 240 K. More recently, Luo et al.[28] have shown the adsorption of nonanoic acid by measuring the surface pressure as a function of the nonanoic acid concentration under acidic and basic conditions. They have also shown by alchemical calculations that nonanoic acid is less acidic in the interfacial region than in the bulk water phase.

From a methodological viewpoint, the modeling of the water–air interface requires considering a two-phase system[29,30] which shows a non-homogeneous density profile along the direction normal to the interface. Many factors have led to these simulations of heterogeneous systems resulting in strong dependencies of the surface tension on size effects, cutoff radius, and long-range corrections but these issues have now been resolved.[31] We modelled the organic molecules (see Fig. 1) since they are representative of the diversity of species observed in cloud droplets and possibly contribute to the formation of an organic film at the surface of cloud/fog droplets. By considering a planar water–air interface, we will investigate the different arrangements of the species in terms of hydrogen bonds, orientation and ability to form clusters. As far as possible, we will try to link these molecular insights with macroscopic properties such as surface tension and free energy. This work represents a proof of concept for evaluating the possible formation of an organic film at the air/water interface in a cloud. It will also enable us to better constrain cloud chemistry models where the formation of an organic film at the interface is not currently considered. This will be the subject of parallel modeling investigations (Renard et al.[32]) in which the effect of this film on the mass
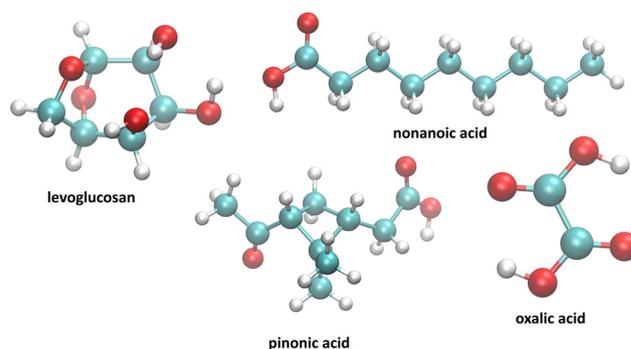

Fig. 1 Set of molecules investigated in this work.

transfer of chemical species (between gaseous and aqueous phases) will be studied.

The paper is organized as follows. Section 2 presents the force field used and the calculation of the surface tension and the free energy along a specific reaction coordinate. We discuss in section 3 the main results of this work from methodological and numerical viewpoints. Finally, in section 4, we draw the main conclusions of this study and potential atmospheric implications.

2 Computational details

2.1 Model

The OPLS-AA force field[33–35] sums intramolecular and intermolecular energy contributions of a molecular system to yield the total configurational energy. The intramolecular interactions consist of bond stretching, angle bending, and dihedral and non-bonded energy contributions as described in eqn (1).

$$U_{\text{intra}} = U_{\text{bond}} + U_{\text{angle}} + U_{\text{torsion}} + U_{\text{nb}} \tag{1}$$

The bond stretching and angle bending energy are described by harmonic potentials defined by eqn (2) and (3), respectively.

$$U_{\text{bond}} = \sum_i k_{\text{b},i} \left(r_i - r_{0,i} \right)^2 \tag{2}$$

$$U_{\text{angle}} = \sum_i k_{\text{b},i} \left(\theta_i - \theta_{0,i} \right)^2 \tag{3}$$

In these equations, k_{b} and k_{θ} are the force constants and r_0 and θ_0 are equilibrium bond and angle values, respectively. The torsional energy is given by

$$U_{\text{torsion}} = \frac{1}{2} \sum_i (V_{1,i}(1 + \cos \phi_i) + V_{2,i}(1 - \cos 2\phi_i)$$
$$+ V_{3,i}(1 + \cos 3\phi_i) + V_{4,i}(1 - \cos 4\phi_i)) \tag{4}$$

where ϕ is the dihedral angle and V_1, V_2, V_3 and V_4 are the Fourier coefficients of each dihedral angle.

The non-bonded interactions between atoms of different molecules give rise to intermolecular interactions and non-bonded interactions occurring between atoms in the same molecule separated by more than three bonds are defined as intramolecular interactions. The specific 1,4-non-bonded intramolecular interactions are scaled by 0.5. These non-bonded interactions sum dispersion–repulsion and electrostatic contributions.

The electrostatic interactions between two charges q_i and q_j at a distance r_{ij} is represented by the Coulomb potential as

$$U_{\text{elect}} = \sum_{i=1}^{N-1} \sum_{j=i+1}^{N} \frac{q_i q_j}{4\pi\varepsilon_0 r_{ij}} \tag{5}$$

where ε_0 represents the dielectric constant of a vacuum. These electrostatic interactions can be calculated by using the Ewald[36] and PPPM[37] methods. The latter consists of making an approximate calculation of the reciprocal space contribution by mapping the system on a mesh and using fast Fourier transform.

Van der Waals interactions are mostly described by the 12-6 Lennard-Jones (LJ) potential as

$$U_{\text{LJ}} = \sum_{i=1}^{N-1} \sum_{j=i+1}^{N} 4\varepsilon_{ij} \left[\left(\frac{\sigma_{ij}}{r_{ij}} \right)^{12} - \left(\frac{\sigma_{ij}}{r_{ij}} \right)^6 \right] \tag{6}$$

where ε_{ij} and σ_{ij} correspond to the energy parameter of the interaction and the Lennard-Jones core diameter. The non-bonded interactions are truncated by using a cutoff radius r_{c}.

The water molecules were modelled by using the SPC/E model.[38] The association of the OPLS-AA model with the SPC/E water model has already been investigated on the free energy of solvation of organic molecules.[39] Agreement with experimental data was also quantitatively demonstrated.[39] Additionally, the SPC/E model was found to reproduce accurately the surface tension of water.[40,41] The LJ parameters for the interactions between unlike sites were calculated by using the Good–Hope combining rules[42,43] which are geometric for $\varepsilon_{ij} = (\varepsilon_{ii}\varepsilon_{jj})^{1/2}$ and $\sigma_{ij} = (\sigma_{ii}\sigma_{jj})^{1/2}$ to be in line with the original version of the OPLS-AA model.[33]

The parametrizations of the selected solute molecules of Fig. 1 defining k_{b}, k_{θ}, r_0, θ_0, V_1, V_2, V_3, V_4, q_i, ε_{ij} and σ_{ij} for each type of interaction are provided by the web-based automatic parameter generators, LigParGen.[44] The partial charges are also provided by LigParGen using the 1.14*CM1A-LBCC method.[45]

2.2 Molecular dynamics

Molecular dynamics simulations were performed by using the LAMMPS package.[46] In all the simulations, the periodic boundary conditions were applied in all three directions. In order to control the temperature, a Nosé–Hoover thermostat was applied[47,48] and the temperature was always set to 290 K to mimic the temperature in the atmosphere.[10] The cutoff distance for van der Waals interactions is set to $r_{\text{c}} = 12.0$ Å, while the particle–particle particle mesh (PPPM) method with an accuracy of 1.0×10^{-4} and a cut-off of 12 Å is considered for the long-range electrostatic interactions. The velocity Verlet integrator was used to integrate the equations of motion using a reduced time step of 1 fs. Each system was first equilibrated as a bulk phase in the NPT statistical ensemble,[49] setting a pressure of 1 atm for 100 ps. This is achieved by combining the hydrostatic equations of Martyna *et al.*[50] with the strain energy proposed by Parrinello and Rahman.[51] Then, vacuum was added on both sides along z for 10 ns; the dimensions of the cell were set to $L_x = L_y = 50$ Å while $L_z = 150$ Å. The acquisition phase was 20 ns long; the configurations were recorded every 20 ps.

802 | *RSC Appl. Interfaces*, 2024, **1**, 800–811

© 2024 The Author(s). Published by the Royal Society of Chemistry

2.3 Potential of mean force and umbrella sampling (US)

The potential of mean force (PMF)[52] also called the free energy profile $F(\xi)$ can be defined as the reversible work to be supplied to two particles which are infinitely-separated to bring them to a contact separation distance. $F(\xi)$ is related to the probability density function $P(\xi)$ of the reaction coordinate ξ as

$$F(\xi) = -\frac{1}{\beta}\ln P(\xi) \tag{7}$$

The probability density function $P(\xi)$ is expressed as

$$P(\xi) = \frac{\int \exp(-\beta \mathscr{U}(\boldsymbol{r}^N))\left(\delta(\xi(\boldsymbol{r}^N)-\xi)\right)d\boldsymbol{r}^N}{Q_{NVT}} \tag{8}$$

The Dirac delta function $\delta(\xi(\boldsymbol{r}^N) - \xi)$ means that we are effectively integrating over all coordinates $\boldsymbol{r}$ such that $\xi(\boldsymbol{r}^N) = \xi$. $\xi(\boldsymbol{r}^N)$ is a vector-valued function of the Cartesian coordinates describing the degrees of freedom of interest.

In the umbrella sampling (US) formalism,[53] a biasing potential $w_i(\xi)$ is added to the Hamiltonian to guide the simulations along a defined reaction coordinate toward a reference ξ_i^{ref}. The calculation is then organized in a series of simulations with different points or windows. The biasing potential takes the form of a harmonic function of strength K to ensure sampling in all regions of ξ. Its operational expression is given by

$$w_i(\xi) = \frac{1}{2}K\left(\xi - \xi_i^{ref}\right)^2 \tag{9}$$

The total biased energy then sums $\mathscr{U}(\boldsymbol{r}^N)$ and $w_i(\xi)$. The biased distribution function $P(\xi)_i^{biased}$ of the ith window is given by

$$P(\xi)_i^{biased} = \exp(-\beta w_i(\xi))\frac{P(\xi)}{\langle \exp(-\beta w_i(\xi))\rangle} \tag{10}$$

The corresponding unbiased $F_i(\xi)$ of the ith window is expressed as

$$F_i(\xi) = -\frac{1}{\beta}\ln P(\xi)_i^{biased} - w_i(\xi) + F_i \tag{11}$$

where the constant F_i defined by eqn (12) could be solved by an iteration process by using the weighted histogram analysis method (WHAM).[54,55]

$$\exp(\beta F_i) = \langle \exp(\beta w_i(\xi))\rangle \tag{12}$$

2.4 Surface tension

The surface tension γ, originally given by Kirkwood and Buff,[56] is defined by

$$\gamma = \frac{1}{2}\langle p_N - p_T\rangle L_z \tag{13}$$

where p_N and p_T are the normal and tangential components of the pressure and L_z is the length of the simulation cell in the z direction. Since a two phase simulation with periodic boundary conditions consists of two interfaces; the surface tension calculated from eqn (13) is divided by 2. For a planar interface, p_N is given by p_{zz}, whereas the tangential component p_T is given by $\frac{1}{2}\left(p_{xx} + p_{yy}\right)$. This expression gives a scalar but does not verify that the system is in mechanical equilibrium.

Irving and Kirkwood[56–61] have shown that γ can be calculated from $p_N(z)$ and $p_T(z)$, the components of the pressure tensor as a function of z:

$$\gamma = \frac{1}{2}\int_{-L_z/2}^{L_z/2}(p_N(z) - p_T(z))dz \tag{14}$$

This local definition of γ, based on the mechanical route, uses the force acting across a unit area in the z-plane for one interface. There is no unique way of calculating the forces across a particular area, since it is unclear which atoms contribute to this force. This has no effect on $p_N(z)$ but different choices of the contour can affect the definition of $p_T(z)$. However, these choices have no effect on the integral in eqn (14). We use here the Harasima definition[56,58,62] for the normal and tangential pressure components. The normal component of the pressure tensor can be written as

$$p_N(z) = \langle p(z)\rangle k_B T$$
$$+ \frac{1}{2\mathscr{A}\Delta z}\left\langle \sum_{i=1}^{N-1}\sum_{j=i+1}^{N}\left(z_{ij}(f_{ij})_z\right) \times \left(\delta(z-z_i) + \delta(z-z_j)\right)\right\rangle \tag{15}$$

where $\mathscr{A}$ is the surface area, Δz is the thickness of the slab and $\rho(z)$ is the local number density. The simulation box is divided into N_z slabs of thickness δz. $\boldsymbol{f}_{ij}$ is the force between atoms i and j defined as:

$$\boldsymbol{f}_{ij} = -\frac{r_{ij}}{r_{ij}}\frac{d\mathscr{U}(r_{ij})}{dr_{ij}} \tag{16}$$

where $\mathscr{U}$ represents all the intramolecular and intermolecular energy contributions. The tangential component of the pressure tensor is then expressed as follows:

$$p_T(z) = \langle \rho(z)\rangle k_B T$$
$$+ \frac{1}{4\mathscr{A}\Delta z}\left\langle \sum_{i=1}^{N-1}\sum_{j=i+1}^{N}\left(x_{ij}(\boldsymbol{f}_{ij})_x + y_{ij}(\boldsymbol{f}_{ij})_y\right) \times \left(\delta(z-z_i) + \delta(z-z_j)\right)\right\rangle \tag{17}$$

These equations indicate that half of the virial contributions arising between atom i and atom j are assigned to the slab where i is located and the other half to the slab where j is located.

© 2024 The Author(s). Published by the Royal Society of Chemistry

RSC Appl. Interfaces, 2024, **1**, 800–811 | **803**

Eqn (13) and (14) should lead to the same value of γ. Indeed, we observe that the two definitions lead to maximum deviations of 0.3 mN m^{-1} which are within the statistical uncertainties of the simulation. Since we used a truncated spherical LJ potential, we need to apply a long-range correction to the surface tension called here γ_{LRC} and expressed as[63]

$$\gamma_{LRC} = \frac{\pi}{2}(\rho_l - \rho_v)^2 \int_0^1 ds \int_{r_c}^{+\infty} dr \coth\left(\frac{2rs}{d}\right) \times \frac{dU_{LJ}^{12,6}}{dr} r^4 (3s^3 - s) \tag{18}$$

where ρ_l and ρ_v represent the densities of the liquid and vapor phases of water, respectively. d is an estimation of the thickness of the interface and s is a parameter defined as $s = (z_i - z_j)/r_{ij}$. The values of ρ_l, ρ_v and d are obtained by assuming that the density profile of water $\rho(z)$ can be fitted to a hyperbolic tangent function of width d.

$$\rho(z) = \frac{1}{2}(\rho_l + \rho_g) - \frac{1}{2}(\rho_l - \rho_g)\tanh(2(z - z_g)/d) \tag{19}$$

By using the SPCE model for water,[38] we found that the tail correction to the surface tension was equal to 3.9 mN m^{-1}.

3 Results and discussion

3.1 Specific arrangements at the interface

In order to describe the water–air interface, we propose to plot in Fig. 2 the density profiles of water and organic molecules in the direction normal to the water surface at $T = 290$ K. We also add the atomic density profiles of oxygen atoms of the organic molecules. These simulations consider a total of 10 organic molecules for the simulation cell. We focus on only one interface for the sake of simplicity. These profiles clearly show two types of behaviour at the interface: (i) an adsorption peak followed by homogeneous distribution in the bulk phase of water and (ii) an adsorption peak at the water surface with only a very small fraction of organic molecules in the water solution.

More specifically, oxalic acid and levoglucosan molecules dissolve in water with a slight predominance at the interface. The presence of a slight peak of adsorption indicates that the organic molecules begin their hydration process before gradually entering the water bulk phase.[64] Concerning the oxalic acid, the density profiles contrast with those obtained at lower temperatures[26] ranging from 200 to 240 K. Actually, at these low temperatures, the density profiles exhibit only an adsorption layer of oxalic molecules at the ice surface while still suggesting a broadening of this layer as the temperature is increasing. It means that the desorption process has already started at 240 K, leading to the presence of a much less pronounced layer at 290 K with a majority of oxalic molecules dissolved in the bulk water. The analysis of the atomic profiles of oxygen atoms provides insight about the structure of the molecule. Indeed, for hydrophilic molecules such as levoglucosan and oxalic acid, the
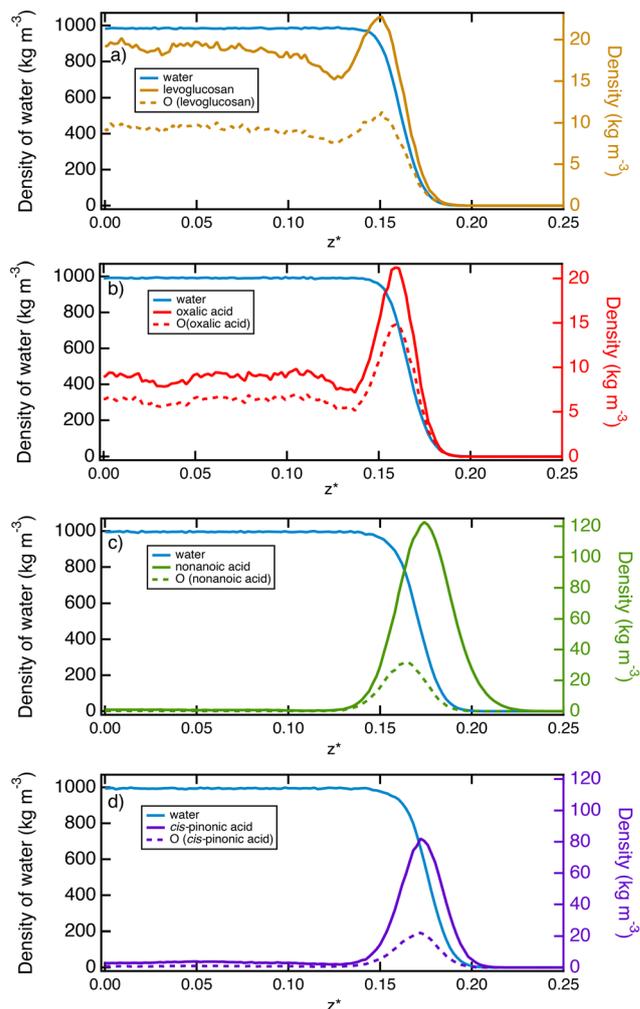

Fig. 2 Molecular density profiles of the liquid–vapor interface of water modified by the addition of 10 organic molecules such as (a) levoglucosan, (b) oxalic acid, (c) nonanoic acid and (d) *cis*-pinonic acid. The density profiles of the organic molecules are read on the right-hand axis. The profiles were calculated as a function of the reduced position z^* defined by z/L_z in the direction normal to the interface. One of both interfaces is shown for clarity. The dotted lines refer to the density profiles of the oxygen atoms of the organic molecules and should be read on the right-hand axis.

hydrophilic parts are distributed on both sides of the molecule's skeleton, which explains why the peak of adsorption of the oxygen atoms is not shifted in relation to that of the molecule.

In contrast, nonanoic and *cis*-pinonic acids are partitioned to the surface and form a kind of hydrophobic coating at the surface with only a tiny fraction of these molecules which sample the region of the bulk water phase. The density profiles of Fig. 2 show two well-separated phases as observed for the oxalic acid at lower temperatures.[26] For the nonanoic acid, the hydrophilic part is at one end of the carbon chain. By comparing the peak of adsorption of oxygen atoms with that of the whole molecule, we deduce that the oxygen atoms are positioned in the interfacial region whereas the vapor phase is occupied by the carbon chains.
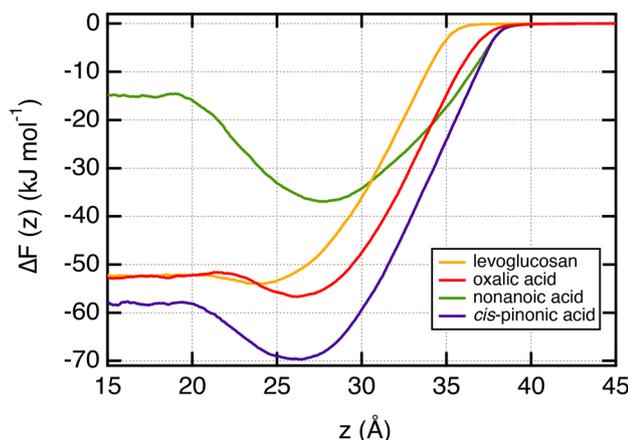
Fig. 3 Free energy profiles $\Delta F(z)$ calculated at T = 290 K for one organic molecule sampling the region from the vapor phase (high z) to the bulk water phase (low z). These profiles were calculated by using the umbrella sampling formalism and refer to the case of infinitely dilute solution.

3.2 Free energy at the interface

In order to characterize the adsorption process of organic molecules on the water surface, we calculate the free energy profiles, also called potential of mean force (PMF), of these organic molecules as a function of the z-position along the direction normal to the interface. These profiles, calculated with the umbrella sampling (US) method, are shown in Fig. 3 for T = 290 K and represent the change of the free energy $\Delta F(z)$ when one organic molecule is moving from the vapor to the bulk water phases. $\Delta F(z)$ = 0 in the vapor phase as the organic molecules do not interact with any water molecules. These free energy profiles confirm the specific arrangements observed from the density profiles. Indeed, the propensity of nonanoic and *cis*-pinonic acids to adsorb at the water surface is confirmed by the negative free minima of $\Delta F(z)$ at the water–air interface, whereas oxalic acid and levoglucosan molecules exhibit only very shallow wells in line with hydrophilic molecules which prefer to stay in water bulk phases. We report in Table 1 the $\Delta F_{\text{water-int.}}$ property which is defined as the free energy gain of moving the molecule from water to the interface. This property ranges from −21.8 to −1.9 kJ mol^{-1}. The organic molecules adsorb preferentially at the interface by forming an organic layer when $\Delta F_{\text{water-int.}}$ is

at least equal to −11.5 kJ mol^{-1}. For values higher than −4.1 kJ mol^{-1}, we observe that the organic molecules are not involved in the hydrophobic adsorption layer. We also report for comparison in Table 1 the polarity index (PI),[65] defined as the ratio between the number of oxygen atoms and carbon atoms of the molecule. Interestingly, only the two smallest PI values give significant free energy minima at the surface of water.

The $\Delta F_{\text{int.-gas}}$ property listed in Table 1 reflects the free energy cost of transferring the organic molecule from the interface to the vapor phase. As expected by the nature of the interactions involved, we observe that this free energy contribution is unfavorable for all the organic molecules studied here, indicating that these molecules prefer either to remain at the interface or to dissolve in the water phase. In addition, nonanoic acid which presents the smaller PI index also yields the smaller $\Delta F_{\text{int.-gas}}$ free energy contribution. From $\Delta F_{\text{water-int.}}$ and $\Delta F_{\text{int.-gas}}$, it is possible to deduce the free energy of solvation $\Delta F_{\text{solv.}}^{\text{PMF}}$ which then corresponds to the transfer of one molecule from the vapor phase to the liquid phase. The $\Delta F_{\text{solv.}}^{\text{PMF}}$ values are collected in Table 1. The free energy of solvation, whether experimental or calculated, can be defined through the Henry's constant K_{H} as

$$\Delta F_{\text{solv.}}^{\text{exp.,calc.}} = -RT \ln RT K_{\text{H}} \tag{20}$$

where K_{H} is expressed in mol m^{-3} Pa^{-1} or mol J^{-1} and R is the perfect gas constant equal to 8.314 kJ mol^{-1} K^{-1}.

For a mono-acid, K_{H} is expressed as

$$K_{\text{H}} = \frac{[\text{AH}] + [\text{A}^-]}{p_{\text{AH}}} = \frac{[\text{AH}]}{p_{\text{AH}}} \left(1 + \frac{K_a}{[\text{H}^+]}\right) \tag{21}$$

whereas the following expression given by eqn (22) applies to a di-acid

$$K_{\text{H}} = \frac{[\text{AH}] + [\text{HA}^-] + [\text{A}^{2-}]}{p_{\text{AH}}} = \frac{[\text{AH}]}{p_{\text{AH}}} \left(1 + \frac{K_{a1}}{[\text{H}^+]} + \frac{K_{a1}K_{a2}}{[\text{H}^+]^2}\right) \tag{22}$$

where p_{AH} is the partial pressure of the acid form, K_a the acidity constant of the mono-acid constant and K_{a1} and K_{a2} the two acidity constants of the di-acid. Since the PMF calculation considers only the acid form, Henry's constant calculated from the PMF curve is defined as

Table 1 Free energy contributions, polarity index and adsorption length calculated with different organic molecules. The values of the free energy are calculated with error bars of ±0.2 kJ mol^{-1}. The definition of these contributions is given in section 3.2. The experimental values of the Henry's law constant can be found in ref. 66 for levoglucosan, ref. 67 for oxalic and nonanoic acids and ref. 68 for *cis*-pinonic acid at ambient temperature. Digits between parentheses indicate the uncertainty in the last significant figure, *i.e.*, 5.0(20) means 5.0 ± 2.0

	$\Delta F_{\text{water-int.}}$ (kJ mol^{-1})	$\Delta F_{\text{int.-gas}}$ (kJ mol^{-1})	$\Delta F_{\text{solv.}}^{\text{PMF}}$ (kJ mol^{-1})	$\Delta F_{\text{solv.}}^{\text{exp.,calc}}$ (kJ mol^{-1})	$\Delta F_{\text{solv.}}^{\text{pH}}$ (kJ mol^{-1})	PI	l_{ads} (nm)
Levoglucosan	−1.9	54.0	−52.1	[−80.4, −64.1]		0.83	0.35(5)
Oxalic acid	−4.1	56.6	−52.5	[−81.3, −38.7]	47.6	2	1.4(2)
Nonanoic acid	−21.8	36.9	−15.1	[−29.7, −22.1]	11.7	0.22	3.4(4) × 10^3
Cis-pinonic acid	−11.5	69.7	−58.2	−49.6	10.4	0.33	44(3)
Nonanoic + levoglucosan	−5.1	60.7					5.0(20)

$$K_H^{PMF} = \frac{[AH]}{p_{AH}} = 1 + 10^{(pH-pK_a)} \quad (23)$$

$$= 1 + 10^{(pH-pK_{a1})} + 10^{(2pH-pK_{a1}-pK_{a2})} \quad (24)$$

where eqn (23) and (24) refer to mono-acid and di-acid, respectively.

$$\Delta F_{solv.}^{PMF} = \Delta F_{solv.}^{exp.,calc.} + RT\ln K_H^{PMF} = \Delta F_{solv.}^{exp.,calc.} + \Delta F_{solv.}^{pH}. \quad (25)$$

The temperature dependence of the free energy of solvation is evaluated through the $d\ln K_H/d(1/T)$ quantity. When this quantity is equal to 9800 for oxalic acid,[66] this indicates that the variation in the free energy of solvation $\Delta F_{solv.}^{298K} - \Delta F_{solv.}^{290K}$ is about +2.8 kJ mol⁻¹. Henry's constant quantifies how the solute is distributed among the bulk liquid water and the bulk vapor.

Given the variety of experimental and predicted Henry's law constant, the possible correction due to the acidity of the solution (see $\Delta F_{solv.}^{pH}$ in Table 1) and the impact of temperature, we observe that the simulated free energy of solvation of the organic molecules agree qualitatively with literature data.

The liquid–vapor interface systems are formed by two components: the chemical substance 1 is water and the substance 2 is the solute defined by the organic molecules. In order to quantify how the solute is distributed among the surface and the bulk liquid water, we can use the adsorption length, defined by

$$l_{ads} = \frac{\sigma_2}{c_{-\infty}} \quad (26)$$

with σ_2 the surface concentration and $c_{-\infty}$ the bulk concentration inside the liquid. σ_2 may be defined as the surface excess of solute quantity relative to water:

$$\sigma_2 = \int_{-\infty}^{z_{Gibbs}} (c(z)-c_{-\infty})dz + \int_{z_{Gibbs}}^{\infty} (c(z)-c_{\infty})dz \quad (27)$$

Here, z_{Gibbs} is the position of the Gibbs dividing interface of water.[69] At equilibrium, the concentration profile is

$$c(z) = c_{\infty}e^{-\Delta F(z)/RT} \quad (28)$$

Therefore, the adsorption length is

$$l_{ads} = \int_{z_{Gibbs}-L_1}^{z_{Gibbs}+L_2} e^{-\frac{\Delta F(z)}{RT}}dz - L_1 e^{-\frac{\Delta F_{solv.}}{RT}} - L_2 \quad (29)$$

where L_1 and L_2 are distances large enough so that $\Delta F(z)$ has reached its plateau value.

The values of l_{ads} are collected in Table 1. l_{ads} ranges from a few angstroms for the most hydrophilic species to a few micrometers for nonanoic acid. This means that most of the molecules of nonanoic acid will be confined to the surface for small droplets where the volume-to-surface ratio is less than or around a micrometer, whereas most of the molecules of levoglucosan or oxalic acid will stay in the bulk of the

droplet. Indeed, the adsorption length represents the thickness of the bulk solution which contains as many solute molecules as the surface. *cis*-Pinonic acid has an intermediate adsorption length.

In the case of our LV system of two components, the Gibbs adsorption isotherm[70] can be written as

$$-d\gamma = \sigma_1 d\mu_1 + \sigma_2 d\mu_2 \quad (30)$$

By positioning the interface at z_{Gibbs} of water, we assume that $\sigma_1 = 0$. At infinite dilutions, where the organic molecules do not interact with each other, we can assimilate the activity a_2 of the component 2 to its concentration c_2. Substituting this into eqn (30) leads to

$$\sigma_2 = -\frac{1}{RT}\frac{d\gamma}{d\ln c_2} = -\frac{c_2}{RT}\frac{d\gamma}{dc_2} \quad (31)$$

At infinite dilutions or low activities, l_{ads} is assumed to be constant. By using $c_2 = c_{-\infty} = \sigma_2/l_{ads}$, the derivative of the surface tension γ with respect to the surface excess σ_2 of the component 2 is simplified as

$$\frac{d\gamma}{d\sigma_2} = -RT \quad (32)$$

The surface excess σ_2 corresponds to the number of molecules per unit area and is expressed in mol m⁻². Eqn (32) means that the enrichment of the solute at the interfacial region leads to a decrease of the surface tension.

From a free energy per unit area viewpoint, Fig. 4 illustrates the dependence of the surface tension of water as
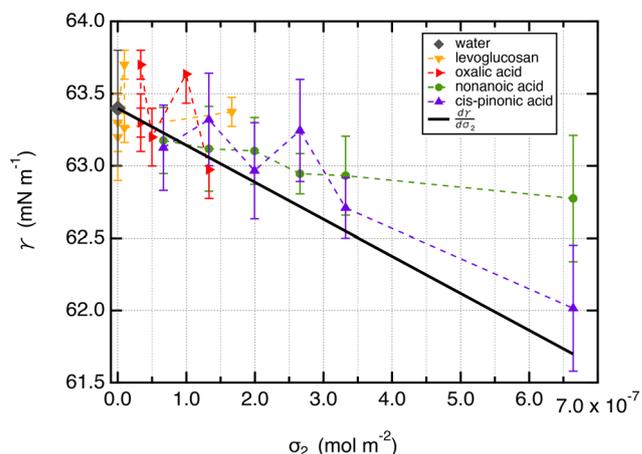
Fig. 4 Surface tension values (mN m⁻¹) of liquid–vapor interfaces of water as a function of the surface excess of organic molecules (σ_2) calculated at 290 K. The surface excess corresponds to a maximum of 10 adsorbed molecules to respect the hypothesis of infinitely dilute solutions. The slope $\frac{d\gamma}{d\sigma_2}$ is equal to –2411 J mol⁻¹ or 0.16 mN m⁻¹ per molecule. The calculations were performed over 5 replicates to consider the statistical fluctuations as accurately as possible.

Table 2 Surface tension values of the liquid–vapor interface of water as a function of the number n of organic molecules and of the surface excess σ_2. n is the number of molecules which can adsorb onto an interface. The simulation box consists of two interfaces and 5000 water molecules. For both interfaces, the number of organic molecules is $2n$. The surface tension was calculated using the mechanical definition by using eqn (15) and (17) with the long-range corrections calculated using eqn (18). The statistical fluctuations and average values of γ were calculated over five independent MD simulations. Digits between parentheses indicate the uncertainty in the last significant figure, *i.e.*, 63.4(4) means 63.4 ± 0.4

	σ_2 (mol m^{-2})	γ (mN m^{-1})	σ_2 (mol m^{-2})	γ (mN m^{-1})	σ_2 (mol m^{-2})	γ (mN m^{-1})	σ_2 (mol m^{-2})	γ (mN m^{-1})
n	Nonanoic acid		*cis*-Pinonic acid		Levuglucosan		Oxalic acid	
1	6.6×10^{-8}	63.2(2)	6.6×10^{-8}	63.1(3)	0	63.2(3)	3.3×10^{-8}	63.3(3)
2	1.3×10^{-7}	63.1(3)	1.3×10^{-7}	63.3(3)	0	63.3(2)	3.3×10^{-8}	63.3(1)
3	2.0×10^{-7}	63.1(2)	2.0×10^{-7}	63.0(3)	0	63.4(1)	3.3×10^{-8}	63.7(1)
4	2.6×10^{-7}	62.9(1)	2.6×10^{-7}	63.2(3)	9.7×10^{-9}	63.7(1)	5.0×10^{-8}	63.2(1)
5	3.3×10^{-7}	62.9(3)	3.3×10^{-7}	62.7(2)	9.7×10^{-9}	63.3(1)	1.0×10^{-7}	63.6(1)
10	6.6×10^{-7}	62.8(4)	6.6×10^{-7}	62.0(4)	1.7×10^{-7}	63.4(1)	1.3×10^{-7}	63.0(2)
20	1.3×10^{-6}	62.8(4)	1.3×10^{-6}	61.1(4)	2.0×10^{-7}	63.2(2)	3.3×10^{-7}	62.9(1)
40	2.6×10^{-6}	63.6(3)	2.6×10^{-6}	59.6(5)	4.0×10^{-7}	63.7(3)	6.0×10^{-7}	63.4(2)

Water
γ = 63.4(4) mN m^{-1}

a function of the surface excess of organic molecules at 290 K. The values of surface tension are listed in Table 2 along with the amount of added organic molecules and surface excess σ_2. We also plot for comparison the $\frac{d\gamma}{d\sigma_2}$ slope of eqn (32) which is equal to 0.16 mN m^{-1} per molecule. We restrict the curve $\gamma = f(\sigma_2)$ to 10 added molecules for each interface in order to respect the assumption of infinitely dilute solutions used to develop the Gibbs adsorption isotherm of eqn (31). First, the surface tension of water at 290 K compares very well with the value calculated from the thermodynamic definition[71] at 298 K using the same model with a deviation less than 1%. The impact of temperature ΔT = 10 K is around 1.5 mN m^{-1} which remains within the uncertainties of the calculation.[71]

Second, for *cis*-pinonic and nonanoic acid molecules which show significant positive surface excess values, Fig. 4 shows that the surface tension decreases with the surface excess as expected from the Gibbs equation. The simulated surface tension of water with *cis*-pinonic acid molecules reproduces very well the theoretical slope. For nonanoic acid, a decrease of surface tension with respect to σ_2 is observed, but the agreement with the theoretical prediction is less quantitative especially for the largest surface excess. Let us recall that the slope corresponds to only 1.6 mN m^{-1} for 10 added molecules at an interface with an area of 50 Å × 50 Å. This result agrees with previous simulations carried out on a water droplet[10] which predict a decrease of 1.3 mN m^{-1} for 10 added *cis*-pinonic acid molecules. This weak decrease of surface tension over the 1–10 range of added molecules is at the limit of the accuracy of the methodology used for the calculation of γ even if γ was calculated over several replicates.

For levoglucosan and oxalic acid molecules, all added molecules dissolve in water and a few remain at the interface. We estimated the number of molecules at the surface of water from the integration of the density profiles in the interfacial region and then calculated the surface excess. By

reporting the surface tension as a function of the surface excess, we observe that the surface tension does not change over this range of σ_2 values within the statistical fluctuations.
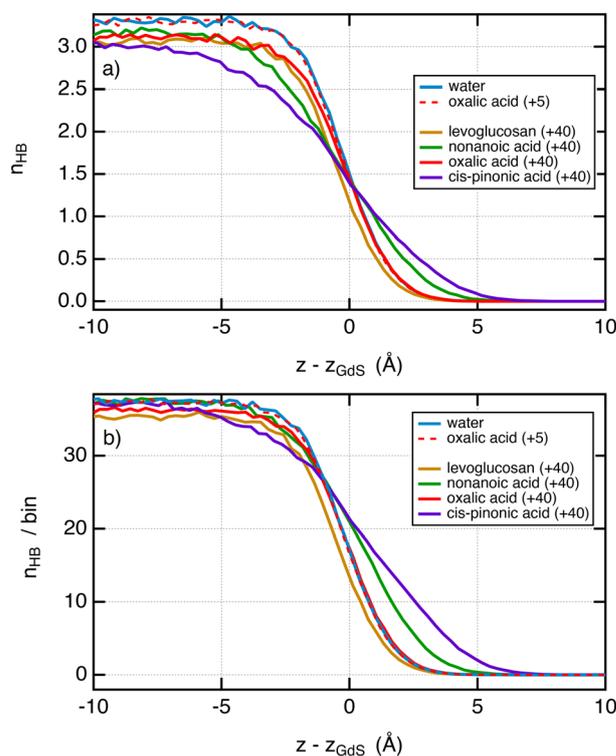
Fig. 5 (a) Profiles of hydrogen bonds between water molecules as a function of the position from the interface. The z-positions were scaled so that the position of the Gibbs dividing surface is located at z = 0 for the interface of the right-hand side. The criteria used to select a hydrogen bond have been taken from ref. 73. Two water molecules are chosen as being hydrogen bonded only if the distance (O–H⋯O) between the donor and the acceptor is less than 2.5 Å and simultaneously the angle O–H⋯O is greater than 150°. (b) Number of total hydrogen bonds involving water–water, water–organic and organic–organic molecules per bin. The bin thickness is 0.3 Å. We used the same criteria of distance and angle.

© 2024 The Author(s). Published by the Royal Society of Chemistry

RSC Appl. Interfaces, 2024, **1**, 800–811 | **807**

Now, it is interesting to analyse the evolution of the surface tension in light of that of the hydrogen bonds in the system. Fig. 5a shows the number of hydrogen bonds between water molecules as a function of the position to the interface. First, we do not observe significant changes in the profiles of hydrogen bonds between pure water and systems with small surface excess values. We show for illustration in Fig. 5a the profile of hydrogen bonds with 5 oxalic acid molecules which matches very well with that of pure water. This is in line with a surface tension that has not changed over this range of σ_2. When the amount of molecules added is greater, e.g. 40, the profiles of hydrogen bonds[72] between water molecules are dependent on the organic molecule. If we pay attention to the only organic molecule which leads to a decrease of the surface tension, i.e. the cis-pinonic and nonanoic acid molecules, we observe that the hydrogen bond profiles have features different from other profiles, namely, a significant smaller number of hydrogen bonds on the liquid side of the interfacial region and a larger number of hydrogen bonds on the vapor side of the liquid–vapor interface. For these acids, the thickness of the interface has been significantly increased compared to oxalic acid and levoglucosan molecules. Fig. 5b shows the profiles of hydrogen bonds between all the species per bin. By summing all the possible hydrogen bonds, this figure supports the conclusions drawn from Fig. 5a and further establishes that the width of the interface has been increased with the cis-pinonic acid and to a lesser extent with the nonanoic acid. This increase of the interfacial thickness is in line with a decrease of the surface tension as reported by the van der Waals theory of surface tension.[72] The explanation of the drop in surface tension with the number of cis-pinonic acid molecules is more complex than it seems and cannot be explained only by the reduction in the number of hydrogen bonds between water molecules as suggested by previous studies.[10]
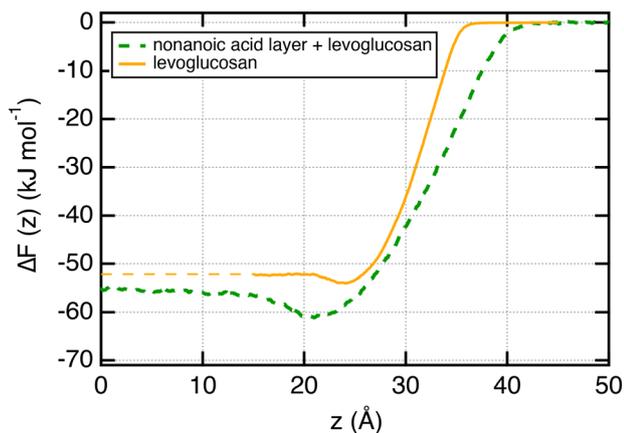
3.3 Hydrophobic layer of nonanoic acid

We now focus on the adsorption of levoglucosan on a layer of nonanoic acid molecules at the surface of water. To do so, we calculate the potential of mean force (PMF) of one molecule of levoglucosan on a monolayer of 40 nonanoic molecules. This free energy profile is shown in Fig. 6 along with the profile of levoglucosan calculated at the surface of pure water. Interestingly, we observe a deeper well depth at the surface as it is saturated with nonanoic acid. Indeed, the well depth increases from −1.9 to −5.1 kJ mol^{-1} (see Table 1).

It means that the presence of nonanoic acid at the interface attracts also the levoglucosan molecules. This is also supported by the value of the adsorption length of levoglucosan which increases by one order of magnitude (from 0.35 to 5.0 nm in Table 1) in the presence of nonanoic acid. This study shows that the presence of some acids with a small PI index at the interface can help the adsorption of more hydrophilic molecules at the surface of water that would not be effective at the surface of pure water.

We complete this study by doing standard MD simulations of the surface of water when it is saturated with nonanoic acid molecules. In this case, we investigate a system of ten levuglucosan and 80 nonanoic acid molecules. A typical equilibrium configuration is given in Fig. 7. This configuration shows the formation of a layer of nonanoic acids with the oxygen atoms pointing towards the water phase and levoglucosan molecules that can sample both the interfacial region and the bulk water phase. The density profiles shown in Fig. 8 confirm the specific arrangements at the interface, namely a hydrophobic monolayer of nonanoic acids with oxygen atoms positioned more on the inside of the water and a more marked adsorption peak of levoglucosan, if we refer to the peak of Fig. 2a, which is accompanied by a smaller fraction of levoglucosan in the water phase.
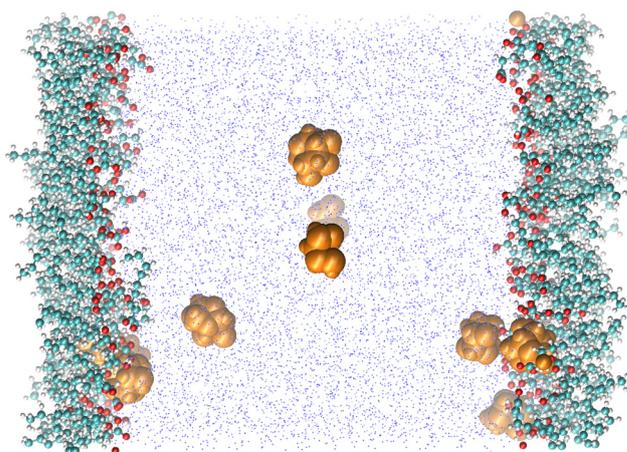

Fig. 6 Free energy profiles $\Delta F(z)$ calculated along the direction normal to the interface for one molecule of levoglucosan which migrates from the vapor to liquid phases. The dotted blue curve corresponds to the profile where the surface of water is saturated by 40 nonanoic acid molecules. The PMFs were calculated by using the US method.

Fig. 7 Snapshot of a typical configuration of a system formed by two interfaces each saturated with 40 nonanoic acid molecules. Ten levoglucosan molecules represented by van der Waals spheres are then added to the system.
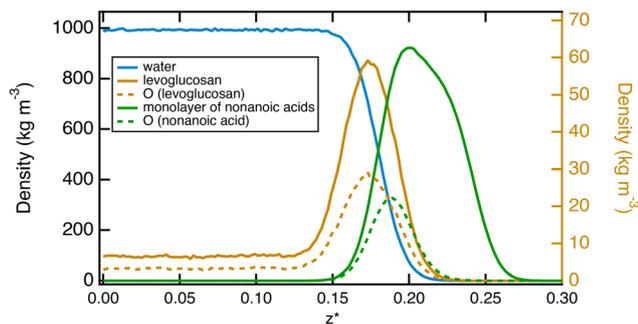
Fig. 8 Density profiles as a function of the reduced z^* position for water, levoglucosan and nonanoic acids as the surface of water is covered by 40 nonanoic molecules. The atomic profiles of oxygen atoms of levoglucosan and acid molecules are represented by dotted lines. The density profiles of levoglucosan and its oxygen atoms are read on the right-hand axis, while the other density profiles are read on the left-hand axis.

4 Conclusions

The objective of this study was to provide a molecular-level understanding of the surface of water with different organic molecules detected in cloud waters and presenting contrasting polar and hydrophobic properties. We applied two-phase molecular simulations to investigate the structural and energetic properties of the liquid–vapor interface of water in the presence of levoglucosan and oxalic, nonanoic and cis-pinonic acids.

The analysis of the molecular density profiles of levoglucosan and oxalic acid molecules at 290 K established that these molecules have a weak inclination for the interface while being dissolved in water. This relatively weak inclination for the water surface is also supported by the presence of shallow wells in the free energy profiles at the interface.

The nonanoic and cis-pinonic acid molecules preferred to accumulate on the surface of water. forming then a hydrophobic monolayer. The free energy profile calculated by moving the organic molecule from the gas phase to the center of the bulk water phase confirmed these specific arrangements from an energy viewpoint. Indeed, nonanoic and cis-pinonic acids exhibited free energy minima at the water surface of −21.8 and −11.5 kJ mol^{-1}, respectively. We also observed that the surface tension of the liquid–vapor interface of water with these two acids decreases with respect to the surface excess of the solute as expected from the Gibbs adsorption isotherm. For levoglucosan and oxalic acid molecules, no dependence of the surface tension on the amount of organic molecules was underlined since these molecules dissolve in water. The profiles of the hydrogen bond of the cis-pinonic and nonanoic acids along the normal direction to the water surface differ from those of the levoglucosan and oxalic acid molecules.

We completed this study by focusing on a surface of water saturated by nonanoic acid molecules. The potential of the mean of a molecule of levoglucosan moving from the gas phase to the water by passing by the interfacial region

established that the well depth of the free energy becomes deeper at the interface when it is covered with nonanoic acid molecules. These results confirmed the fact that the accumulation of organic molecules at the interface depends not only on the hydrophilic nature of the molecules but also on the composition of the interfacial region.

Molecular simulation is an effective tool for rationalizing the interfacial properties of water in the presence of organic molecules. This study also proposes to reconsider how a cloud chemistry model takes into account interfacial properties. Currently, those models consider only the reactivity of compounds in bulk phases and a kinetic parametrization of the mass transfer of molecules. They need to be better constrained to consider the presence of an organic film at the droplet surface and its effect on this mass transfer and the possible heterogeneous reactivity.

Author contributions

Conflicts of interest

There are no conflicts to declare.

Acknowledgements

Notes and references

1 A. M. Deal, R. J. Rapf and V. Vaida, *J. Phys. Chem. A*, 2021, **125**, 4929–4942.

2 J. S. Rowlinson and B. Widom, *Molecular Theory of Capillarity*, Clarendon Press, Oxford, 1982.

3 G. J. Gittens, *J. Colloid Interface Sci.*, 1968, **30**, 406–412.

4 J. J. Jasper, *J. Phys. Chem. Ref. Data*, 1972, **1**, 841–1009.

5 G. Vasquez, E. Alvarez and J. M. Navaza, *J. Chem. Eng. Data*, 1995, **40**, 611–614.

6 A. B. A. Bianco, L. Deguillaume, M. Vaïtilingom, E. Nicol, J.-L. Baray, N. Chaumerliac and M. Bridoux, *Environ. Sci. Technol.*, 2018, **52**, 10275–10285.

7 C. M. Salvador, T.-T. Ho, C. C.-K. Chou, M.-J. Chen, W.-R. Huang and S.-H. Huang, *Atmos. Environ.*, 2016, **140**, 565–575.

8 B. Nozière, M. Kalberer, M. Claeys, J. Allan, B. D'Anna, S. Decesari, E. Finessi, M. Glasius, I. Grgić, J. F. Hamilton, T. Hoffmann, Y. Iinuma, M. Jaoui, A. Kahnt, C. J. Kampf, I.

© 2024 The Author(s). Published by the Royal Society of Chemistry

RSC Appl. Interfaces, 2024, **1**, 800–811 | **809**

Kourtchev, W. Maenhaut, N. Marsden, S. Saarikoski, J. Schnelle-Kreis, J. D. Surratt, S. Szidat, R. Szmigielski and A. Wisthaler, *Chem. Rev.*, 2015, **115**, 3919–3983.

9 S. Hornik, J. Sykora, J. Schwarz and V. Zdimal, *ACS Omega*, 2020, **5**, 22750–22758.

10 X. Li, T. Hede, Y. Tu, C. Leck and H. Agren, *J. Phys. Chem. Lett.*, 2010, **1**, 769–773.

11 K. A. Wokosin, E. L. Schell and J. A. Faust, *Environ. Sci.: Atmos.*, 2022, **2**, 775–828.

12 J. Reid, T. Eck, S. Christopher, R. Koppmann, O. Dubovik, D. Eleuterio, B. Holben, E. Reid and J. Zhang, *Atmos. Chem. Phys.*, 2005, **5**, 827–849.

13 K. T. Valsaraj, G. J. Thoma, D. D. Reible and L. J. Thibodeaux, *Atmos. Environ., Part A*, 2010, **27**, 203–210.

14 S. Rossignol, L. Tinel, A. Bianco, M. Passananti, M. Brigante, D. J. Donaldson and C. George, *Science*, 2016, **353**, 699–702.

15 M. F. Ruiz-Lopez, J. S. Francisco, M. T. C. Martins-Costa and J. M. Anglada, *Nat. Rev. Chem.*, 2020, **4**, 459–475.

16 M. T. C. Martins-Costa and M. F. Ruiz-López, *J. Am. Chem. Soc.*, 2023, **145**, 1400–1406.

17 N. Hayeck, I. Mussa, S. Perrier and C. George, *ACS Earth Space Chem.*, 2020, **4**(8), 1247–1253.

18 K. Valsaraj, G. Thoma, D. D. Reible and L. Thibodeaux, *Atmos. Environ.*, 1993, **27**, 203–210.

19 W. Seidl, *Atmos. Environ.*, 2000, **34**, 4917–4932.

20 S. E. Schwartz, in *Chemistry of multiphase atmospheric systems*, Springer, Berlin, Heildelberg, 1986, pp. 415–471.

21 M.-C. G. Chalbot, J. Brown, P. Chitranshi, G. Gamboa Da Costa, E. D. Pollock and I. G. Kavouras, *Atmos. Chem. Phys.*, 2014, **14**, 6075–6088.

22 G. Engling, P. Herckes, S. Kreidenweis and J. Collett Jr., *Atmos. Environ.*, 2006, **40**, 2959–2972.

23 S. Enami, M. R. Hoffmann and A. J. Colussi, *J. Phys. Chem. Lett.*, 2017, **8**, 3888–3894.

24 G.-L. Hou, J. Zhang, M. Valiev and X.-B. Wang, *Phys. Chem. Chem. Phys.*, 2017, **19**, 10676–10684.

25 X. Huang, J. Zhang, B. Luo, J. Luo, W. Zhang and Z. Rao, *Atmos. Environ.*, 2019, **198**, 133–141.

26 M. Darvas, S. Picaud and P. Jedlovszky, *Phys. Chem. Chem. Phys.*, 2011, **13**, 19830–19839.

27 M. Darvas, S. Picaud and P. Jedlovszky, *ChemPhysChem*, 2010, **11**, 3971–3979.

28 M. Luo, N. A. Wauer, K. J. Angle, A. C. Dommer, M. Song, C. M. Nowak, R. E. Amaro and V. H. Grassian, *Chem. Sci.*, 2020, **11**, 10647–10656.

29 F. Goujon, P. Malfreyt, A. Boutin and A. H. Fuchs, *Mol. Simul.*, 2001, **27**, 99–114.

30 A. Ghoufi and P. Malfreyt, *J. Chem. Phys.*, 2012, **136**, 024104.

31 A. Ghoufi, P. Malfreyt and D. J. Tildesley, *Chem. Soc. Rev.*, 2016, **45**, 1387–1409.

32 P. Renard, J. Devémy, A. Dequidt, P. Malfreyt and L. Deguillaume, in preparation.

33 W. L. Jorgensen, D. S. Maxwell and J. Tirado-Rives, *J. Am. Chem. Soc.*, 1996, **118**, 11225–11236.

34 W. L. Jorgensen and J. Tirado-Rives, *Proc. Natl. Acad. Sci. U. S. A.*, 2005, **102**, 6665–6670.

35 M. Robertson, J. Tirado-Rives and W. Jorgensen, *J. Chem. Theory Comput.*, 2015, **11**, 3499–3509.

36 P. P. Ewald, *Ann. Phys.*, 1921, **369**, 253–287.

37 J. W. Eastwood, R. W. Hockney and D. N. Lawrence, *Comput. Phys. Commun.*, 1980, **19**, 215–261.

38 H. J. C. Berendsen, J. R. Grigera and T. P. Straatsma, *J. Phys. Chem.*, 1987, **91**, 6269–6271.

39 D. Vassetti, M. Pagliai and P. Procacci, *J. Chem. Theory Comput.*, 2019, **15**, 1983–1995.

40 S. P. Kadaoluwa Pathirannahalage, N. Meftahi, A. Elbourne, A. C. Weiss, C. F. McConville, A. Padua, D. A. Winkler, M. Costa Gomes, T. L. Greaves and T. C. Le, *et al.*, *J. Chem. Inf. Model.*, 2021, **61**, 4521–4536.

41 P. Malfreyt, *Mol. Simul.*, 2014, **40**, 106–114.

42 H. A. Lorentz, *Ann. Phys.*, 1881, **12**, 127–136.

43 D. Berthelot, *C. R. Hebd. Seances Acad. Sci.*, 1898, **126**, 1703–1855.

44 L. S. Dodda, I. Cabeza de Vaca, J. Tirado-Rives and W. L. Jorgensen, *Nucleic Acids Res.*, 2017, **45**, 331–336.

45 L. S. Dodda, J. Z. Vilseck, J. Tirado-Rives and W. L. Jorgensen, *J. Phys. Chem. B*, 2017, **121**, 3864–3870.

46 S. Plimpton, *J. Comput. Phys.*, 1995, **117**, 1–19.

47 S. Nosé, *Mol. Phys.*, 1984, **52**, 255–268.

48 W. G. Hoover, *Phys. Rev. A: At., Mol., Opt. Phys.*, 1985, **31**, 1695.

49 S. Melchionna, G. Ciccotti and B. Lee Holian, *Mol. Phys.*, 1993, **78**, 533–544.

50 G. J. Martyna, D. J. Tobias and M. L. Klein, *J. Chem. Phys.*, 1994, **101**, 4177–4189.

51 M. Parrinello and A. Rahman, *J. Appl. Phys.*, 1981, **52**, 7182–7190.

52 J. G. Kirkwood, *J. Chem. Phys.*, 1935, **3**, 300–313.

53 G. M. Torrie and J. P. Valleau, *J. Comput. Phys.*, 1977, **23**, 187–199.

54 S. Kumar, J. M. Rosenberg, D. Bouzida, R. H. Swendsen and P. A. Kollman, *J. Comput. Chem.*, 1992, **13**, 1011–1021.

55 B. Roux, *Comput. Phys. Commun.*, 1995, **91**, 275–282.

56 J. G. Kirkwood and F. P. Buff, *J. Chem. Phys.*, 1949, **17**, 338–343.

57 J. H. Irving and J. Kirkwood, *J. Chem. Phys.*, 1950, **18**, 817–829.

58 J. S. Rowlinson and B. Widom, *Molecular Theory of Capillarity*, Clarendon Press, Oxford, 1982.

59 J. P. R. B. Walton, D. J. Tildesley, J. S. Rowlinson and J. R. Henderson, *Mol. Phys.*, 1983, **48**, 1357–1368.

60 J. P. R. B. Walton, D. J. Tildesley, J. S. Rowlinson and J. R. Henderson, *Mol. Phys.*, 1983, **50**, 1381.

61 K. Shi, E. E. Santiso and K. E. Gubbins, *J. Chem. Phys.*, 2021, **154**, 084502.

62 A. Harasima, *Advances in Chemical Physics*, Wiley & Sons, 1958, pp. 203–237.

63 E. M. Blokhuis, D. Bedaux, C. D. Holcomb and J. A. Zollweg, *Mol. Phys.*, 1995, **85**, 665–669.

64 A. Ghoufi and P. Malfreyt, *Phys. Chem. Chem. Phys.*, 2010, **12**, 5203–5205.

65 B. Xing, W. B. McGill and M. J. Dudas, *Environ. Sci. Technol.*, 1994, **28**, 1929–1933.

66 C. Qin, Y. Gou, Y. Wang, Y. Mao, H. Liao, Q. Wang and M. Xie, *Atmos. Chem. Phys.*, 2021, **21**, 12141–12153.

67 R. Sander, *Atmos. Chem. Phys.*, 2023, **23**, 10901–12440.

68 H. Lignell, S. A. Epstein, M. R. Marvin, D. Shemesh, B. Gerber and S. Nizkorodov, *J. Phys. Chem. A*, 2013, **117**, 12930–12945.

69 H.-J. Butt, K. Graf and M. Kappl, *Physics and Chemistry of Interfaces*, John Wiley & Sons, 2003.

70 H.-J. Butt, K. Graf and M. Kappl, *Physics and chemistry of interfaces*, John Wiley & Sons, 2023.

71 C. Vega and E. de Miguel, *J. Chem. Phys.*, 2007, **126**, 154707.

72 R. Lovett, P. W. DeHaven, J. Vieceli, J. James and F. P. Buff, *J. Chem. Phys.*, 1973, **58**, 1880–1885.

73 A. Luzar and D. Chandler, *Phys. Rev. Lett.*, 1996, **76**, 928–931.

© 2024 The Author(s). Published by the Royal Society of Chemistry

RSC Appl. Interfaces, 2024, **1**, 800–811 | **811**